Journal Pre-proof

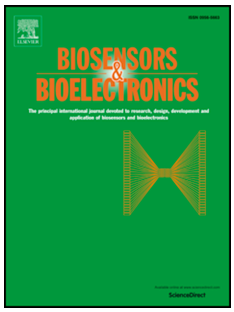

Fabrication of ultra-sensitive photoelectrochemical aptamer biosensor: Based on semiconductor/DNA interfacial multifunctional reconciliation via 2D-C_3N_4

Yang Li, Yuyu Bu, Fengqiu Jiang, Xianying Dai, Jin-Ping Ao

PII: S0956-5663(19)30982-0

DOI: https://doi.org/10.1016/j.bios.2019.111903

Reference: BIOS 111903

To appear in: *Biosensors and Bioelectronics*

Received Date: 1 October 2019

Revised Date: 4 November 2019

Accepted Date: 17 November 2019

Please cite this article as: Li, Y., Bu, Y., Jiang, F., Dai, X., Ao, J.-P., Fabrication of ultra-sensitive photoelectrochemical aptamer biosensor: Based on semiconductor/DNA interfacial multifunctional reconciliation via 2D-C_3N_4, *Biosensors and Bioelectronics* (2019), doi: https://doi.org/10.1016/j.bios.2019.111903.

$BiVO_4$/2D-C_3N_4 Synthesis and Characterization, Y.L. and F.Q.J.; X.Y.D., J.P.A. and Y.L. performed data analysis and interpreted the experimental results; Project Design and Direction, Y.Y.B.; All authors proofread, commented on, and approved the final version of this manuscript for submission.

Fabrication of ultra-sensitive photoelectrochemical aptamer biosensor: based on semiconductor/DNA interfacial multifunctional reconciliation via 2D-C_3N_4

Yang Li, Yuyu Bu*, Fengqiu Jiang, Xianying Dai*, Jin-Ping Ao

Key Laboratory of Wide Band-Gap Semiconductor Materials and Devices, School of Microelectronics, Xidian University, Xi'an, 710071, China

ABSTRACT: In this work, we fabricate a novel bismuth vanadate/two dimensional-carbon nitride/deoxyribonucleic acid ($BiVO_4$/2D-C_3N_4/DNA) aptamer photoelectrochemical (PEC) sensor, and this sensor provides a record detection sensitivity area (5×10^{-7} μg/L - 10 μg/L) for Microcystin-LR (MC-LR). Meanwhile, except for MC-LR detection, this sensor presents highly sensitivity for tumor marker, heavy metal ion, antibiotic also by changing the DNA aptamer. Photo charge dynamic and theory calculation results reveal that 2D-C_3N_4 is a key material for multifunctional interface reconciliation of this PEC aptamer sensor. Firstly, it can serve as photogenerated hole oriented-transfer medium from the $BiVO_4$ photoanode to the detective target; In addition, 2D-C_3N_4 with large area of π electron cloud can fix the DNA aptamer parallelly by π-π bonding with the nucleic acid in the DNA aptamer to shorten the hole transfer distance from the semiconductor to target. So that, a record MC-LR detection sensitivity has been achieved by the 2D-C_3N_4 modified $BiVO_4$/DNA aptamer sensor.

KEYWORDS: PEC aptamer biosensor; 2D-C_3N_4 interlayer; Semiconductor/DNA interface reconciliation; Ultrahigh sensitivity; Charge transfer

1. Introduction

Semiconductor photoelectrochemical (PEC) sensor can detect the target molecules quantitatively via the photoinduced electron transfer between the n-type semiconductor and the target interface (Zhao et al., 2014; Zhou et al., 2015). Because of the difference between excitation signal (photons) and the detection signal (current signal), the semiconductor PEC sensor presents the advantages of low background signal, high sensitivity, simple operating instrument and low detection cost (Wu et al., 2018; Freeman et al., 2013). Consequently, it has displayed important application prospect in the fields of environmental risk substance monitoring and biomedical detection.

The early PEC sensors are generally linked with the drawbacks of poor specificity, low sensitivity and weak resistance to interfering signal (Tian et al., 2014). To solve these problems, researchers have focused on the integration of the biotechnology and PEC sensor technology. At present, the biosensor techniques mainly include enzyme-linked immunosorbent assay (ELISA), molecular imprinting technique and DNA aptamer technique (Liu et al., 2009). Of them, the DNA aptamer technique is fix the random oligonucleotide DNA sequence on the surface of a semiconductor PEC sensor and the aptamer is used as the front end detection probe to capture the detective target specifically, thus inducing gradient changes on the photocurrent signal of the sensor with the concentration of the target increasing gradually (Ng et al., 2012). Compared with molecular imprinting technique and ELISA, the PEC/DNA aptamer technique processes higher theoretical limit on sensitivity, specificity and environmental stability, which shows well application potential in the field of detection.

Currently, the performance of PEC/DNA aptamer sensor is mainly limited by the disharmonious semiconductor/DNA interface, which influences the directional photocarrier transfer process and DNA aptamer molecule fixation. These problems inhibit the detection sensitivity, stability and specificity of the PEC/DNA aptamer sensor. Consequently, to develop the multifunctional materials for DNA aptamer fixing and to orient

the photogenerated hole transfer between semiconductor and DNA interface simultaneously are very significance, which is becoming the current research difficulty also.

Graphite-phase carbon nitride (g-C_3N_4) is a typical layered graphite-like polymer semiconductor, after exfoliation, it can be reduced to 2D-like structure (Tan et al., 2017). The triazine ring fabricating by C and N atoms in the 2D structure will form the highly delocalized π conjugated system through sp^2 hybridization, providing a possibility to fix the DNA molecule on it by π=π bond adsorption because of the π conjugated on the nucleotide (Chang et al., 2018). Meanwhile, an II type heterojunction can be formed between $BiVO_4$ and 2D-C_3N_4 after compositing, owing to the energy band potential difference (Wang et al., 2017; Song et al., 2018). Thus, the photogenerated holes producing by $BiVO_4$ will transfer to 2D-C_3N_4 directionally by the II type heterojunction controlling, then transfer to the detective targets (who capture by the well fix DNA aptamer) to generate an oxidation current. So, 2D-C_3N_4 presents the potential to reconcile the semiconductor/DNA interface from multiple angles to solve the core question of PEC/DNA aptamer sensor.

In this paper, a $BiVO_4$/2D-C_3N_4 photoanode with II type heterojunction structure was prepared by modifying the ultrathin 2D-C_3N_4 onto the surface of $BiVO_4$ photoanode. The II type heterojunction provided an electric field to transfer the photogenerated holes producing by $BiVO_4$ to the 2D-C_3N_4, enhancing the oriented transfer capacity of photogenerated holes to the detective target. Meanwhile, 2D-C_3N_4 could fix the DNA aptamer probe by the large area π-π adsorption property, thus closing the space distance between the photogenerated holes on 2D-C_3N_4 to the detective target. As a result, the PEC aptamer sensor showed an excellent detection property for MC-LR molecule with a ultra-low LOD of 4.191×10^{-8} μg/L. MC-LR is an important biomarker producing by cyanobacteria propagation with highly toxic for concentration. The significance of MC-LR detection is not only for water safety, but also for the lag stage monitoring of the cyanobacteria outbreak (Preece et al., 2017; Huisman et al., 2018). Thus, this sensor provides a possibility on early warning of algae outbreak in lake, which is a universal and difficult problem. In addition, by changing the DNA aptamers, the $BiVO_4$/2D-C_3N_4 PEC sensors presented high sensitivities for tumor markers, heavy metal ions and antibiotics also, so, it is a universal PEC sensor with large application width.

2. Experimental and theoretical calculation

2.1 Materials and reagents

Bismuth nitrate pentahydrate ($Bi(NO_3)_3 \cdot 5H_2O$), sodium iodide (NaI), vanadyl acetylacetonate ($C_{10}H_{14}O_5V$), ethylene diamine tetraacetic acid (EDTA), were obtained from Aladdin Chemical Reagent Co., Ltd., China. p-Benzoquinone ($C_6H_4O_2$), Hg solution (100 μg/ml, 5 % HNO_3), tetracycline ($C_{22}H_{24}N2O_8$) and dopamine hydrochloride ($C_8H_{11}NO_2 \cdot HCl$) were obtained from Macklin Chemical Reagent Co., Ltd., China. Fluorine doped tin oxide (FTO) electrodes (10 mm × 20 mm × 1.6 mm, Sheet resistance<15 Ω) were obtained from Zhuhai Kaivo Optoelectronic Technology Co., Ltd., China. Microcystin-LR and microcystin-RR were purchased from Puhuashi Technology Development Co., Ltd., China. The MC-LR aptamer (the sequence of 5′-GGCGCC AAA CAG GAC CAC CAT GAC AAT TAC CCA TAC CACCTC ATT ATG CCC CAT CTC CGC-3′), Hg^{2+} aptamer (TTC TTT CTT CCC TTG TTG GTT), tetracycline aptamer (CGT ACG GAA TTC GCT AGC CCC CCG GCA GGC CAC GGC TTG GGT TGG TCC GAC TGC GCG TGG ATC CGA GCT CCA CGT G), dopamine aptamer (GTC TCT TGC GCC AGA GAA CAC TGG GGC AGA TAT GGG CCA GCA CAG AAT GAG GCC C), were synthesized by Sangon Biotech Co., Ltd., China. Standard microcystins solutions with various concentrations were prepared by dissolving microcystins samples in 50 mM Tris-HCl buffer (pH 7.4, 0.2 M KCl, 0.1 M NaCl, 5 mM $MgCl_2$ and 1 mM EDTA) to obtain various concentrations of microcystins. The aptamer solution was received by centrifuging at 4000 rpm for 40 s, and dissolving it into Tris-HCl buffer. All solutions were prepared using Milli-Q grade water (Millipore water purification system Z18 MΩ, Milli-Q, Millipore, Billerica, MA). All the reagents were used as received.

2.2 Synthesis of $BiVO_4$/2D-C_3N_4

1.4452 g $Bi(NO_3)_3 \cdot 5H_2O$ and 5.9956 g NaI were dissolved into 100 ml ultrapure water to adjust the solution pH to 1.2; afterwards, ethanol solution containing 0.3 M p-benzoquinone was added, and the obtained solution was used to electrodeposition BiOI film electrode. Moreover, the dimethyl sulfoxide solution containing 0.15 M vanadyl acetylacetonate was coated onto the BiOI film, and the $BiVO_4$ film electrode could

be obtained after drying and thermal insulation for 1 h at 450 °C. The 2D-C_3N_4 powder was prepared according to the method reported in previous literature (Tian et al., 2017). the obtained powder was ultrasonic treated for 6 h in the mixture of 50 mL ethanol and 150 mL ultrapure water, then, the white supernatant was obtained after centrifugation. 50 μL 2D-C_3N_4 dispersion liquid was collected and coated onto the prepared $BiVO_4$ film, dry and annealing at 250 °C for 30 min to obtain the $BiVO_4$/2D-C_3N_4 photoanode.

2.3 Fabrication of PEC/DNA aptamer sensor

Fig. 1A presents the structure and preparation process of the PEC aptamer sensor designed in this paper. To be specific, the buffer containing 3 μM MC-LR aptamer was coated onto the prepared $BiVO_4$/2D-C_3N_4 film electrode and dried at 37 °C for 2 h; thereafter, the electrode surface was washed with ultrapure water to obtain the $BiVO_4$/2D-C_3N_4/DNA aptamer electrode. Afterwards, MC-LR solutions at different concentrations (5×10^{-7} μg/L, 1×10^{-6} μg/L, 1×10^{-5} μg/L, 1×10^{-4} μg/L, 0.0025 μg/L, 0.05 μg/L, 1 μg/L, 10 μg/L) were coated onto the prepared $BiVO_4$/2D-C_3N_4/aptamer detection electrode to incubate at constant temperature for 30 min, and then the electrode surface was washed, followed by natural drying for further photoelectric detection.

2.4 Apparatus

Atomic force microscope (AFM) was used to characterize the electrode surface micrographics (Bruker Dimension Icon, 5500LS, Keysight Technologies Inc, America). X-ray diffraction (XRD, D/MAX-2500/PC, Rigaku Co., Tokyo, Japan) was used to detect the crystal phase of $BiVO_4$. The morphologies and elemental mapping of the electrode materials were investigated using FE-SEM (FE-SEM, Ultra 55, Zeiss, Germany), and a field emission transmission electron microscope (FE-HRTEM, JEM-2100F, JEOL Ltd., Japan).

Photoelectrochemical performance measurements were performed at a Zahner Zennium pro Electrochemical Workstation (Zahner, Germany) in a traditional three-electrode cell containing 0.1M phosphate buffer solution (PBS, pH 7.4) with Ag/AgCl as reference electrode and a piece of platinum as counter electrode, respectively. Control intensity modulated photocurrent/photovoltage spectroscopy (CIMPS/CIMVS) was measured to calculate the electron transport time and electron lifetime of series photoanodes. The electron transit time (τ_r), electron lifetime (τ_{rec}) and charge transfer efficiency (η_{ct}) can be obtained by the following

formula (Yalavarthi et al., 2019).

$$\tau_r = \frac{1}{2\pi f_{CIMPS}} \quad (1)$$

$$\tau_{rec} = \frac{1}{2\pi f_{CIMVS}} \quad (2)$$

$$\eta_{ct} = \frac{LFI}{HFI} \quad (3)$$

where f_{CIMPS}/f_{CIMVS} is the frequency of the minimum imaginary component in CIMPS/CIMVS measurements, LFI is low-frequency intercept, HFI is high-frequency intercept in the first quadrant of CIMPS.

The detection limit (LOD) of sensor can be calculated by the formula (Zhang et al., 2010).

$$Lod=3S_b/k \quad (4)$$

where S_b is standard deviation of blank sample, k is slope of the calibration curve (plot of photocurrent intensity vs. the the logarithm of MC-LR concentration).

2.5 Computational models and methodology

In this paper, a 3 × 3 single-layer 2D-C_3N_4 calculation model was constructed, among which, the single-layer g-C_3N_4 model was basically constructed through segmentation along the primitive cells (001) (P. Li et al., 2017). Besides, $BiVO_4$ (010) was used as the calculation surface, which was mainly because that (010) was the major exposure surface of m-$BiVO_4$; besides, it was suggested in previous research that, g-C_3N_4 could be stably adsorbed onto the $BiVO_4$ (010) surface (Zhang et al., 2015). The absorption energies of the 2D-C_3N_4 and $BiVO_4$ (010) crystal surfaces on the nucleotides where cytosine (C), thymine (T), guanine (G) and adenine (A) were calculated. All calculations were carried out basing on the periodic density functional theory (DFT) calculations by using the cambridge sequential total energy package (CASTEP) model in Materials Studio 2017, which with the generalized gradient approximation (GGA) using the perdew-burke-ernzerhof (PBE) functional. For valence electrons, a plane-wave basis set was employed with a cut-off at 400 eV and the Monkhorst-Pack grid was 4×4×4 k-point. The electronic minimization parameter of the total energy/atom convergence tolerance was 5.0×10^{-5} eV (Melissen et al., 2016). The adsorption energy was calculated as follows.

$$\Delta E_G = E_{gM} - E_g - E_M \quad (5)$$

Where E_{gM} is the total energy of the adsorption system, E_g represents the 2D-C_3N_4 or $BiVO_4$ energy before adsorption, and E_M stands for the energy of nucleotides where four basic groups (A, T, G and C) are located.

3. Results and discussion

3.1 Morphology characterization of PEC/DNA aptamer sensor surface

Fig. S1A shows the SEM surface microstructure of $BiVO_4$ film. A porous nanostructure fabricating by twisted rod-like particles can be observed with a nonuniform length from 140 nm~290 nm. **Fig. S1B** and **S1C** show the low and high revolution SEM images of $BiVO_4$ surface after 2D-C_3N_4 modification. We can find that lamellar substances with the diameters ranging from 80 nm~150 nm were occurred on the surface of $BiVO_4$ particles. **Fig. S1D** displays the XRD spectra of $BiVO_4$ and $BiVO_4$/2D-C_3N_4. From this figure, $BiOV_4$ (m-$BiVO_4$) peak can be observed, but no C_3N_4 diffraction peak can be detected, because of the trace content of 2D-C_3N_4 on the surface of $BiVO_4$. However, from the energy dispersive spectrometer (EDS) spectra (**Fig. S1E**), we can get the information that elements C and N are obviously increased on the $BiVO_4$ surface after 2D-C_3N_4 modification, indicating the presence of C_3N_4. Figure 1B presents the SEM images of $BiVO_4$/2D-C_3N_4/DNA aptamer. Compared with the surface morphology of $BiVO_4$/2D-C_3N_4 (**Fig. S1C**), a large amount of DNA granular tissues are found on the 2D-C_3N_4 surface, which closely attach onto the $BiVO_4$/2D-C_3N_4 surface to form a favorable contact. TEM was performed to further analyze the $BiVO_4$ and 2D-C_3N_4 morphology. **Fig. S1F** shows the HRTEM images of $BiVO_4$, from which the (0 4 0) plane of $BiVO_4$ is observed with a lattice distance 0.17 nm. **Fig. S2G** demonstrates that the surface of $BiVO_4$ is evenly cladded by 2D-C_3N_4 layer with a thickness ~5 nm and formed well interfacial contact. However, no lattice fringe can be observed from the HRTEM image of 2D-C_3N_4 (**Fig. S1H, I**), which phenomenon mainly relates to the low crystallinity of the 2D-C_3N_4.

Fig. 1C presents the AFM surface morphology of the pure $BiVO_4$. the $BiVO_4$ surface displays undulating tissues obviously with a roughness R_q of 58 nm. **Fig. 1D** shows the surface morphology of $BiVO_4$ after 2D-

C_3N_4 modification. Compared with the pure $BiVO_4$ surface, the roughness degree slightly reduces to 55 nm, because of the flexible 2D-C_3N_4 cladding. **Fig. 1E** shows the surface morphology of $BiVO_4$/2D-C_3N_4 after DNA aptamer modification. It can get the information that the roughness of the thin film is markedly decreased to 51 nm. The main reason is that the DNA aptamer molecule with a length of 20 nm and a thickness of 2 nm (**Fig. S2**) are sufficiently fixed onto the surface of $BiVO_4$/2D-C_3N_4 photoanode under the adsorption via π-π bond between 2D-C_3N_4 and DNA aptamer, so that the surface roughness decreases largely. After MC-LR targets capturing, As shown in **Fig. 1F**, its surface was slightly bulged, which is mainly induced by the MC-LR embedding into the aptamer helical structure, leading to a slight increase of the surface roughness to 53.8 nm.

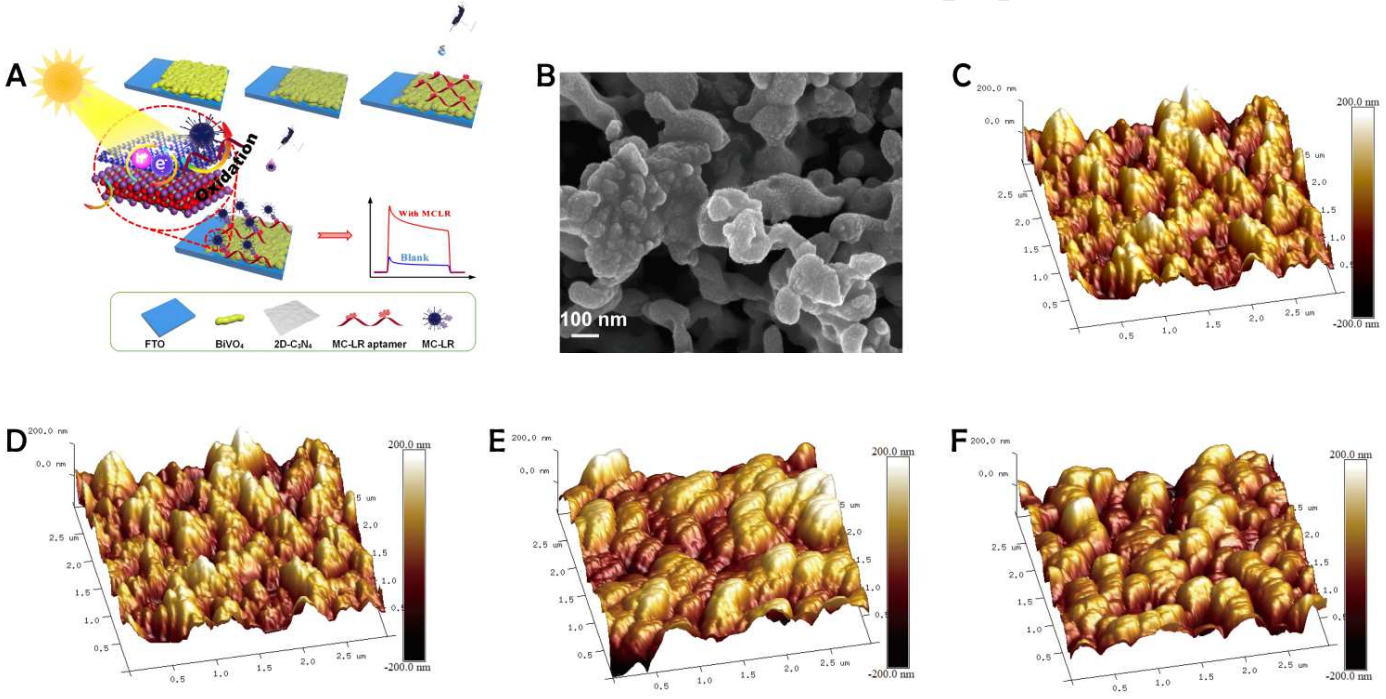

Fig. 1. (A) Schematic diagram of PEC/DNA aptasensor and the mechanism for MC-LR detection. (B) SEM images of $BiVO_4$/2D-C_3N_4/DNA aptamer. (C) AFM images of $BiVO_4$ thin film. (D) AFM images of $BiVO_4$/2D-C_3N_4 thin film. (E) AFM images of $BiVO_4$/2D-C_3N_4/DNA aptamer thin film. (F) AFM images of $BiVO_4$/2D-C_3N_4/DNA aptamer with 0.995 μg/L MC-LR (20 μL) thin film.

3.2 Characterization of PEC/DNA aptamer sensor for MC-LR

Fig. S3A ~ D show the photoinduced IT and IV curves of $BiVO_4$ photoanode and 2D-C_3N_4 modified $BiVO_4$ photoanodes with various modification contents and annealing temperatures. It can be seen that the

photocurrent density of $BiVO_4$ photoanode is increased after 2D-C_3N_4 modification. The optimal photocurrent is achieved by 50 μL 2D-C_3N_4 dispersion liquid covering and annealing at 250 °C. **Fig. 2A** reveals the photocurrent responses of various MC-LR concentrations with an applied bias potential 0.05 V (vs. Ag/AgCl), and the photocurrent density increases gradually with the MC-LR concentration increasing. **Fig. S4A ~ D** show the photocurrent density changing with MC-LR detection concentrations gradient increasing at the applied bias potentials of -0.1 V, -0.05 V, 0 V, and 0.1 V (vs. Ag/AgCl), respectively. Meanwhile, based on the results providing in Figure S5A~D, the corresponding linearity degrees of $BiVO_4$/2D-C_3N_4/DNA aptamer sensors for MC-LR detection are further transformed. As shown in **Fig. 2B**, it can be seen that for the same MC-LR target concentration, there is a difference on photocurrent changes (slope of the detection line) inducing by applied bias potentials changing. Typically, a larger slope of the detection line means a higher sensitivity of the sensor. When the bias potentials set at -0.1 V and -0.5 V, the photocurrents of the sensors are suppressed completely, so, their slope values smaller than that of at the bias potential of 0 V. The greatest detection line slope is achieved at the applied bias potential +0.05 V, suggesting that this is most optimal bias potential of the PEC $BiVO_4$/2D-C_3N_4/DNA aptamer sensor for MC-LR target detection, and the linear detection area is 5×10^{-7} μg/L~10 μg/L. Nonetheless, the sensor has completely lost the linear detection characteristic when the bias potential up to +0.1 V further, indicating that the forward bias potential can move ahead the chemical potential for the photocurrent saturation, thereby decreasing the upper-limit concentration for MC-LR detection. **Fig. 2C** shows the detection calibration line regarding to the logarithmic MC-LR concentration with the photocurrent response value at the optimal bias potential of +0.05 V, meaning a well reproducibility of the PEC $BiVO_4$/2D-C_3N_4/DNA aptamer sensor. **Fig. 2D** shows The variation of photocurrent response for different concentrations of MC-LR, photocurrent response for 5×10^{-8} μg/L compared with blank in Fig. 2E The limit of detection (LOD) was estimated to be 4.191×10^{-8} μg/L (S/N = 3). To the best of our knowledge, compared with the published literatures on MC-LR detection sensor, as shown in Table 1, the sensor LOD achieved in this paper exceeds two orders of magnitudes relative to the previously reported best result (Liu et al., 2019; Zervou et al., 2017; Tang et al., 2019; Wei et al., 2018; Tan et al., 2015; Lee and Son, 2019; Chen et al., 2012; Chen et al., 2018; Liu et al., 2017; Du et al., 2016), meaning that a new detection record is achieved by this PEC $BiVO_4$/2D-C_3N_4/DNA

aptamer sensor. Apart from the ultrahigh detection sensitivity, the sensor designed in this paper possesses superb specificity also. The specificity of the sensors was carried out under the same experimental conditions using a 0.995 μg/L MC-LR as target, meanwhile, the equivalent mass concentrations of MC-RR (microcystin congeners), Pb^{2+}, Hg^{2+}, Norfloxacin, and bovine serum albumin (BSA) were used as the interference sources, respectively. As shown in **Fig. 2F**, the results indicate that the detection photocurrent is responded obviously only in the presence of MC-LR, while there are not obvious photocurrent signals for other interference sources.

Table 1. Comparison of the present and other reported methods for the MC-LR detection

Number	Method	linear range	LOD	Reference
1	Ultra high pressure liquid chromatography-tandem mass spectrometry (UHPLC-MS/MS)	0.005~10.0 μg/L	4.14×10^{-4} μg/L	Liu et al., 2019
2	Solid-phase extraction and high performance liquid chromatography-tandem mass spectrometry (SPE and LC-MS/MS)	0.034~ 63 μg/L		Zervoua et al., 2017
3	Colorimetric aptasensor	0.05~25 μg/L	0.05 μg/L	Tang et al.,2019
4	Electrical immunoassay	5×10^{-5}~1μg/L	5×10^{-5} μg/L	Wei et al., 2018
		0.001 ~ 1 μg/L	6×10^{-4} μg/L	Tan et al., 2015
5	Fluorescence biosensor	1×10^{-4} ~100 ug/L	1×10^{-4} μg/L	Lee et al., 2019
6	Molecularly imprinted polymers (MIPs)-based lateral flow	0.5~100 ug/L	0.1 μg/L	Chen et al., 2012
		0.001 ~ 0.1 μg/L and 0.1 ~10.0 μg/L	2.3×10^{-4} μg/L	Chen et al., 2018
7	PEC Aptasensor	1×10^{-4} ~ 100 μg/L	3×10^{-5} μg/L	Liu et al., 2017
		1.0×10^{-5}~0.1 μg/L	4.496×10^{-6} μg/L	Du et al., 2016
This Work		**5×10^{-7}~10 μg/L**	**4.191×10^{-8} μg/L**	

Afterwards, the causes for the superb properties of PEC $BiVO_4$/2D-C_3N_4/DNA aptamer sensor were further investigated. **Fig. S4E** shows the photocurrent response signals of $BiVO_4$/DNA aptamer sensor and $BiVO_4$/2D-C_3N_4/DNA aptamer sensor to 0.995 μg/L MC-LR at the detection bias potential of 0.05 V. It can figure out that the photocurrent density of $BiVO_4$/DNA aptamer sensor is much smaller than that of $BiVO_4$/2D-C_3N_4/DNA aptamer sensor, suggesting that 2D-C_3N_4 played a vital role between the interface of $BiVO_4$ and

DNA aptamer, so, the especial function of 2D-C_3N_4 should be revealed carefully.

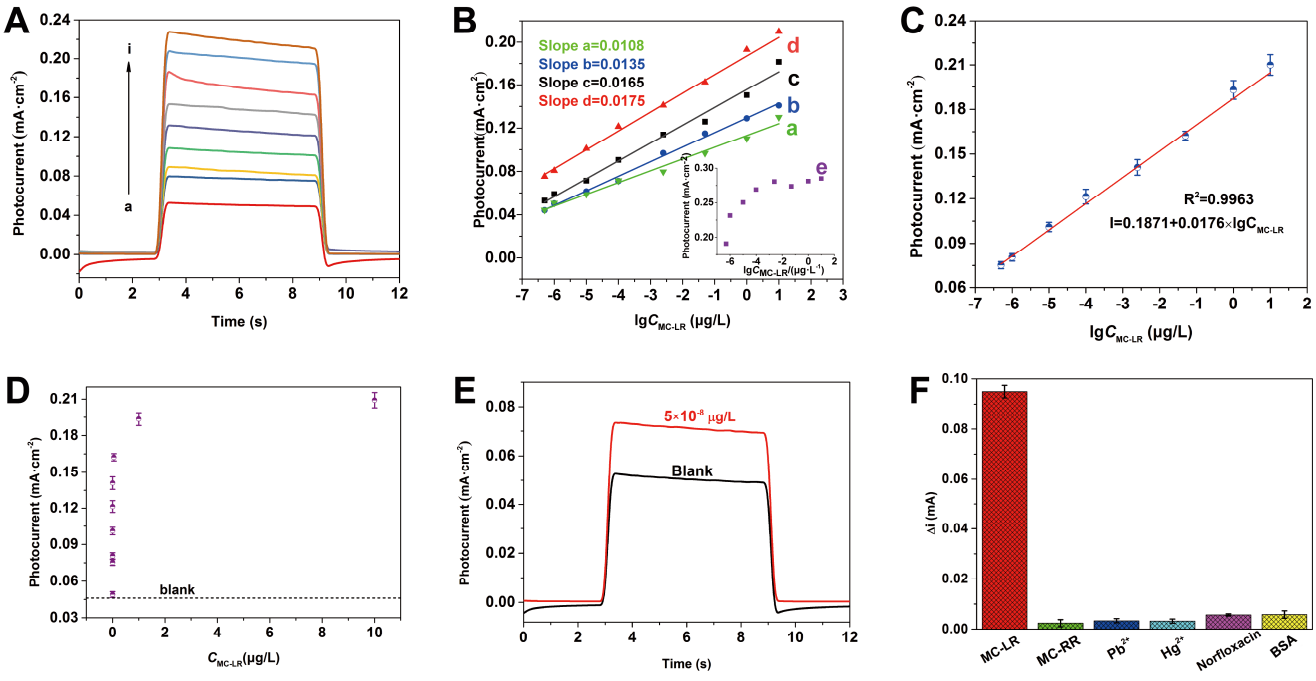

Fig. 2. (A) Photocurrent response for different concentrations of MC-LR: (a) 0, (b) 5×10^{-7}, (c) 1×10^{-6}, (d)1×10^{-5}, (e)1×10^{-4}, (f) 0.0025, (g) 0.05, (h) 1, (i)10 μg/L at potential of 0.05 V (vs. Ag/AgCl). (B) Linear relationship between PEC response of this biosensor and MC-LR concentration at potential of -0.1 V, -0.05 V, 0 V, 0.05 V, 0.1 V (vs. Ag/AgCl). (C) The corresponding liner calibration cure for different concentrations of MC-LR at potential of 0.05 V (vs. Ag/AgCl). (D) The variation of Photocurrent response for different concentrations of MC-LR. (E) Photocurrent response for 5×10^{-8} μg/L compared with blank. (F) Selectivity of the $BiVO_4$/2D-C_3N_4/DNA aptamer sensor.

3.3 Calculation of absorption energy of four bases on $BiVO_4$ or 2D-C_3N_4 surface

The DFT method was employed to calculate the adsorption energies of $BiVO_4$/DNA and 2D-C_3N_4/DNA interfaces, respectively. the interface models of $BiVO_4$/DNA and 2D-C_3N_4/DNA were constructed, as shown in **Fig. 3A and 3C**. To simplify the computational model, DNA was isolated into four kinds of deoxynucleotides, including C, T, G and A. Specifically, these four deoxynucleotides were used to construct the interface models on the $BiVO_4$ (010) plane and 2D-C_3N_4, respectively. Thereafter, the first principles were adopted to

calculate the adsorption behaviors of 2D-C_3N_4 and $BiVO_4$ (010) plane on four various deoxynucleotides. **Fig. 3A** displays the stable model of four deoxynucleotides absorbed onto the 2D-C_3N_4 surface. We can get the information that the bases in deoxynucleotide molecules are adsorbed onto the g-C_3N_4 surface in an almost parallel manner, with distance of about 0.35 nm ~ 0.39 nm between them. **Fig. 3B** presents the absorption energies of 2D-C_3N_4 to four bases. It can be seen that the absorption energies between 2D-C_3N_4 to the 4 bases (A, T, G, C) are located at -1.14 eV, -1.17 eV, -1.00 eV, and -1.06 eV, respectively. Such results demonstrate that the π bond in 2D-C_3N_4 will attract the π bond formed in the carbon-nitrogen hybrid ring in the bases, meanwhile, the electronegative phosphate group on bases will far away from the electronegative 2D-C_3N_4 by the repulsive interaction. **Fig. 3C and 3D** show the stable model and adsorption energy variations of $BiVO_4$ (010) plane to the four deoxynucleotides. The adsorption energies between $BiVO_4$ (010) plane to 4 deoxynucleotides (A: -0.20 eV, T: -0.23 eV, G: -0.11 eV, C: -0.25 eV) are much smaller than those values of 2D-C_3N_4. This result indicates that 2D-C_3N_4 processes much higher combining affinity with DNA. So, after modification it on the surface of $BiVO_4$ photoanode, 2D-C_3N_4 can capture the DNA aptamer efficiently, meanwhile, shorten the space distance between them by parallel π-π adsorption. Under this situation, "glucose-phosphoric acid strain" containing specific "hairpin structure" for MC-RL target capturing will expose on the outermost layer of the PEC $BiVO_4$/2D-C_3N_4/DNA aptamer sensor to capture the MC-RL target directly and efficiently. Furthermore, because of the space distance decreasing between $BiVO_4$/2D-C_3N_4 and DNA aptamer, the distance between $BiVO_4$/2D-C_3N_4 to the captured MC-LR target will shorten also, inducing photogenerated holes transfer distance (from 2D-C_3N_4 to MC-LR target) reducing. Therefore, this is one of the important factors for the sensitivity of PEC $BiVO_4$/2D-C_3N_4/DNA aptamer sensor improving.

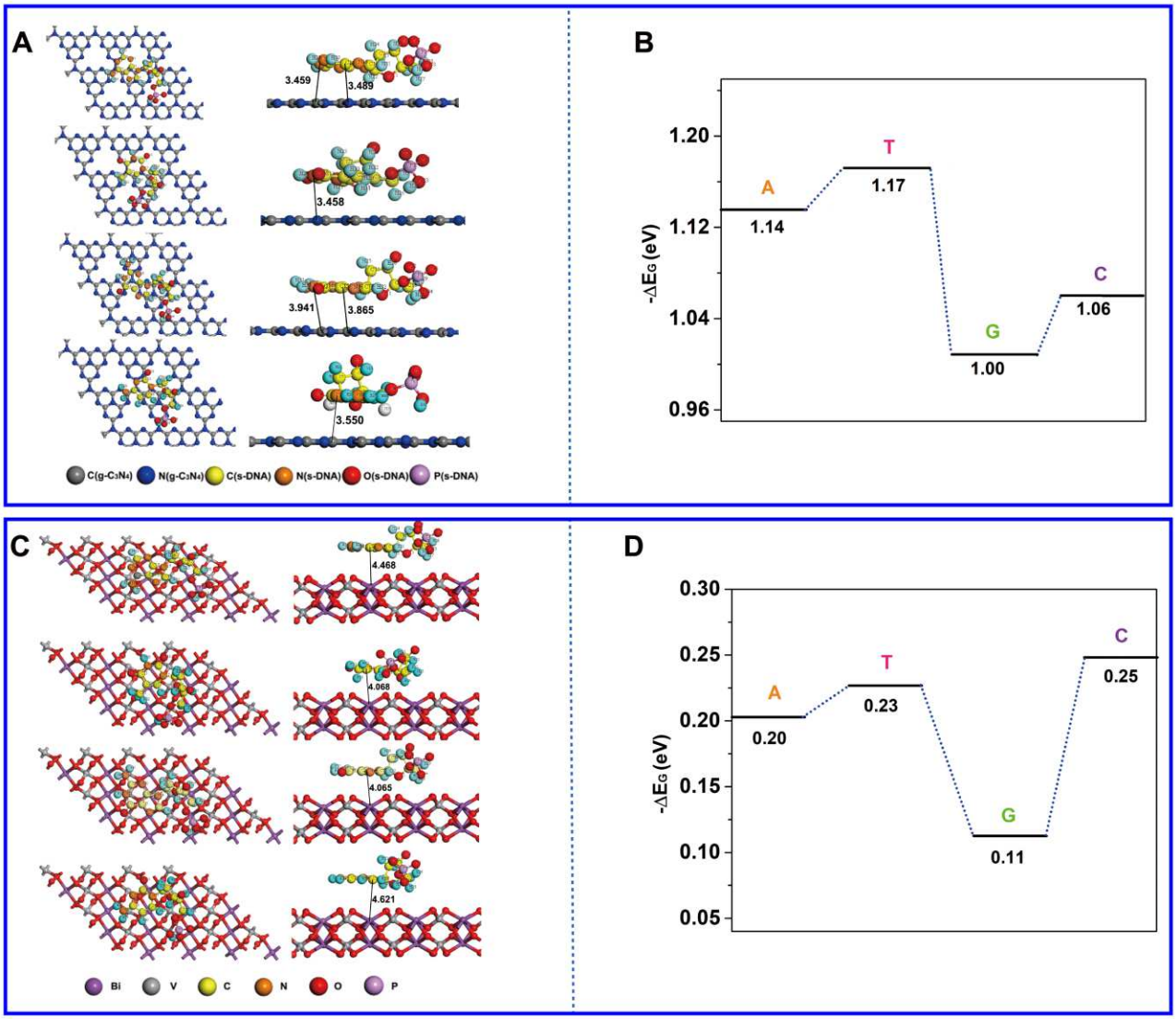

Fig. 3. (A) The optimized geometry of the 2D-C_3N_4/A, T, G, C. (B) Adsorption energy of the 2D-C_3N_4/A, T, G, C. (C) The optimized geometry of the $BiVO_4$/A, T, G, C. (D) Adsorption energy of the $BiVO_4$/A, T, G, C.

3.4 The photogenerated charge transfer mechanism of the PEC/DNA aptamer sensor for MC-LR.

2D-C_3N_4 can optimize the space structure of the PEC $BiVO_4$/DNA aptamer sensor by parallel adsorption of DNA aptamer, additionally, the introduction of 2D-C_3N_4 at the semiconductor/DNA interface has possibility to influence transport dynamics of the photogenerated carriers largely, then improve the performance of the PEC $BiVO_4$/DNA aptamer sensor. Based on the above speculation, it is very important to research the photogenerated carriers transport process in the $BiVO_4$/2D-C_3N_4/DNA aptamer sensor. Electrochemical impedance spectroscopy (EIS) is an effective method to investigate the carrier transport process of a

photoanode. From **Fig. 2B**, we can get the information that PEC $BiVO_4$/DNA aptamer sensor shows the best sensitivity for MC-LR detection at the bias potential 0.05 V, but lost linearity when the bias potential adding to 0.1 V, an obvious difference on charge transport dynamics may be formed under these two bias potentials. So, in this study, 0.05 V and 0.1 V bias potentials were applied under dark and light excitation conditions for EIS testing, respectively. Photoinduced EIS results of the samples presented in **Fig. 4A and 4B**. Corresponding fitting circuit diagram is showed in **Fig. 4C**, in which R_1, R_2 and R_3 are the solution resistance, bulk thin film resistance and surface charge transfer resistance, respectively. The fitting data of each resistance are displayed in Table S1. Under two different tested bias potentials, their resistances show similar variation trend (the dark state resistance changes are presented in **Fig. S5A ~ S5D**. After 2D-C_3N_4 modifying on the surface of $BiVO_4$ photoanode, compared with the pure $BiVO_4$ photoanode, the resistance arc is apparently reduced. Because of the II type n-n heterojunction between $BiVO_4$ and 2D-C_3N_4, the photogenerated holes on the $BiVO_4$ valence band will directly transfer to the π orbit of g-C_3N_4. Meanwhile, the photogenerated electrons on the 2D-C_3N_4 conduction band will transfer to the $BiVO_4$ conduction band rapidly. The matched energy band potentials of these two semiconductors can suppress the recombination of photogenerated electrons and holes effectively, thereby decreasing the EIS arc and enhancing the photocurrent signal. When the $BiVO_4$/2D-C_3N_4 photoanode further modify by DNA aptamer, the DNA aptamer will cover this photoanode surface partially, and the corresponding EIS results under presented in **Fig. 4A (Curve a)** and **Fig. 4B (Curve a)** under bias potential of 0.05 V and 0.1 V, respectively. We can get the information that the charge transfer resistances show an increasing trend obviously, indicating that DNA isn't a good hole transfer material. Thus, when it covered on the surface of $BiVO_4$/2D-C_3N_4 photoanode, it will block the transfer process of the photogenerated holes at the solid-liquid interface. In other words, for the photogenerated holes, they will not select the DNA aptamer as a transfer route to oxidize the captured MC-LR target for detection. However, after the $BiVO_4$/2D-C_3N_4DNA aptamer sensor capturing the MC-LR molecules, as shown in **Fig. 4A (Curve d)** and **Fig. 4B (Curve d)**, the EIS resistances are rapidly decreased, indicating that the DNA aptamer probe can pull the MC-LR targets very close to the $BiVO_4$/2D-C_3N_4 surface because of a short space distance between 2D-C_3N_4 and DNA aptamer.

Therefore, the photo-generated holes producing by $BiVO_4$ and 2D-C_3N_4 can oxidize the space adjacent MC-LR molecules through bypass the DNA aptamer hole barrier layer.

It is well known that the surface electronegativity and steric configuration will be changed on PEC $BiVO_4$/2D-C_3N_4DNA aptamer sensor after capturing MC-LR targets with varying concentrations, inducing EIS resistance changing of the PEC sensor, corresponding results showed in **Fig. 4A (Curve d ~ f)** and **Fig. 4B (Curve d ~ f)**. When the applied bias potential setting at 0.05 V, as illustrated in **Fig. 4A (curve d ~ f)**, the EIS resistances show regular gradient changing with the MC-LR target concentration gradient changing. Under this bias potential, the drifting capacity of photogenerated holes to MC-LR will be controlled by the MC-LR target concentration completely. However, As shown in **Fig. 4B (Curve d ~ f)**, when the applied bias potential increasing to 0.1 V, the EIS resistances are not markedly changed after high concentration of MC-LR target capturing. In this case, the drifting process of photo-generated holes mainly influence by the bias potential, so, the photogenerated holes transfer speed will be easier to saturate under a high MC-LR target captured concentration (> 0.0025 μg/L) compared with 0.05 V , we can see that the concentration of MC-LR to increase (from 0.0025 μg/L to 10 μg/L), the EIS resistances are only slightly declined. This phenomenon keeps consistent with the previously variation trend of the photocurrent showed in **Fig. 2B** completely.

CIMPS and CIMVS are both frequencies dominated testing technologies, in which a bundle of stable DC light coupling a small sinusoidal modulated disturbing light are employed as excitation signal to excite the semiconductor photoelectrode. Then the output signals are the corresponding steady state photocurrent and modulated photocurrent, or the steady state photovoltage and modulated photovoltage. There are four main parameters to describe the photogenerated carrier's kinematic process including electron lifetime and collection efficiency, electron diffusion coefficient and diffusion time. **Fig. 4D** shows the CIMVS testing curves of the sensors. The left side in the figure represents the high frequency region, while the right side is the low frequency region. The vertical coordinate and horizontal coordinate represented the imaginary part and real part of the responding photovoltage, respectively. Typically, the photogenerated electron lifetime τ_{rec} could be calculated according to formula (1). The precise calculation data of electron lifetime of the samples are

presented in **Table S2 (τ_{rec})**. It could be seen from the table that compared with pure $BiVO_4$ photoanode, the II type heterojunction formation in $BiVO_4$/2D-C_3N_4 photoanode can suppress the recombination of the photogenerated electrons and holes, thus extending the electron lifetime. The photogenerated electron lifetime is not changed after DNA aptamer adsorption on the $BiVO_4$/2D-C_3N_4 surface, suggesting that DNA aptamer dose not participate in the photogenerated hole transfer process, which was consistent with previous EIS results showed in **Fig. 4A (Curve b and c)** and **Fig. 4B (Curve b and c)**. After trace MC-LR adsorption onto the electrode surface, the photogenerated electron lifetime of the $BiVO_4$/2D-C_3N_4/DNA aptamer sensor is markedly declined, indicating that MC-LR molecular can capture the photogenerated carriers for redox reaction. However, the CIMVS testing was carried out under the open circuit condition, there is no obvious current passed through the entire circuit, only low concentration of MC-LR target can realize the saturated capture of photogenerated holes. Therefore, as shown by the data in **Table S2 (τ_{rec})**, the electron lifetime would not change with the MC-LR concentration continuous increasing.

Fig. 4D and 4F show the CIMPS test curves of sensors under the bias potentials of 0.05 V and 0.1 V, respectively. The photogenerated charge transfer time in the bulk of thin film could be calculated by formula (2), and the charge transfer efficiency could be calculated according to formula (3). **Table S2 (τ_r)** displays the charge transfer time data under various applied bias potentials. The photogenerated charges transfer time is not affected (keeping at 1.35 ms) before and after 2D-C_3N_4 modification onto the pure $BiVO_4$ photoanode. Such result suggests that because of the 2D-C_3N_4 ultrathin structure and II type heterojunction fabricating with $BiVO_4$, it will not affect the interfacial transfer of photogenerated carrier negatively. After DNA aptamer modify onto the electrode surface, the charge transfer time is extended to 2.90 ms due to the increase in the spatial resistance. After MC-LR targets fixed on the surface of $BiVO_4$/2D-C_3N_4/DNA aptamer sensor, under the bias potential of 0.05 V, the photogenerated holes should bypass the DNA aptamer to react with MC-LR target, inducing charge transfer path increasing, thus increasing the τ_r value further to 3.68 ms. Nonetheless, the τ_r values are kept at 3.68 ms even though increasing the MC-LR target concentration further, because the spatial distance between hole to the target site remained the same. On the other hand, when the applied bias potential

adding to 0.1 V, as presented in **Fig. 4F** and **Table S2,** compared with the τ_r values tested at 0.05 V, the values keep at 2.90 ms until the MC-LR concentration increase to 0.0025 μg/L, indicating that the photogenerated charges transfer process is dominated by the high applied potential, but not the concentrations of MC-LR, because the higher bias potential induced electric field required thicker captured MC-LR molecular layer to shield it, so the detective curve of the $BiVO_4$/2D-C_3N_4/DNA aptamer sensor lost linearity under a higher bias potential 0.1 V.

Furthermore, the charge transfer efficiencies of the PEC $BiVO_4$/2D-C_3N_4/DNA aptamer sensor under various biases were calculated. The results are presented in **Table S2 (η_{ct})**. 2D-C_3N_4 can improve the charge transfer efficiency of $BiVO_4$ photoanode, because of II type heterostructure. Then the charge transfer efficiencies are both decreased after DNA aptamer modification under bias potentials of 0.05 V and 0.1 V, because of the hole transfer steric hindrance of the DNA aptamer. After the adsorption of MC-LR target molecules, the charge transfer efficiencies largely increase to 55.0 % and saturate at near 71.2 % under the bias potential of 0.05 V with the target concentrations increasing from 5×10^{-7} to 10 μg/L. However, as shown in **Table S2**, when the bias potential increasing to 0.1 V, there are not obvious change of the charge transfer efficiencies and keep at 46.2% to 49.7% with the target concentrations increasing. This phenomenon indicates that the high applied bias potential will accelerate the saturation of charge transfer efficiency to cause the concentration of target lost control on this process, thus leading to linear distortion of the PEC $BiVO_4$/2D-C_3N_4/DNA aptamer sensor under too high applied bias potential.

Fig. 4G presents the working mechanism of the $BiVO_4$//DNA aptamer sensor with and without 2D-C_3N_4 modification. Without 2D-C_3N_4 modification, it is hard for the DNA aptamer fixation on the surface of $BiVO_4$ photoanode, inducing weak capture capacity of the MC-LR target molecules. When 2D-C_3N_4 modified on the surface of $BiVO_4$ photoanode, the photogenerated carriers can be separated effectively by the II type heterojunction. Meanwhile, 2D-C_3N_4 can fix the DNA aptamer parallelly by π-π bond adsorption and decrease the spatial distance between 2D-C_3N_4 to DNA aptamer largely. Then the DNA aptamers will capture the MC-LR targets efficiently and pull MC-LR targets to contact with the surface of $BiVO_4$/2D-C_3N_4. In this case, the

photogenerated holes on 2D-C_3N_4 will bypass DNA and transfer to MC-LR target molecule for oxidation depolarization, inducing significant increasing on the photocurrent signal.

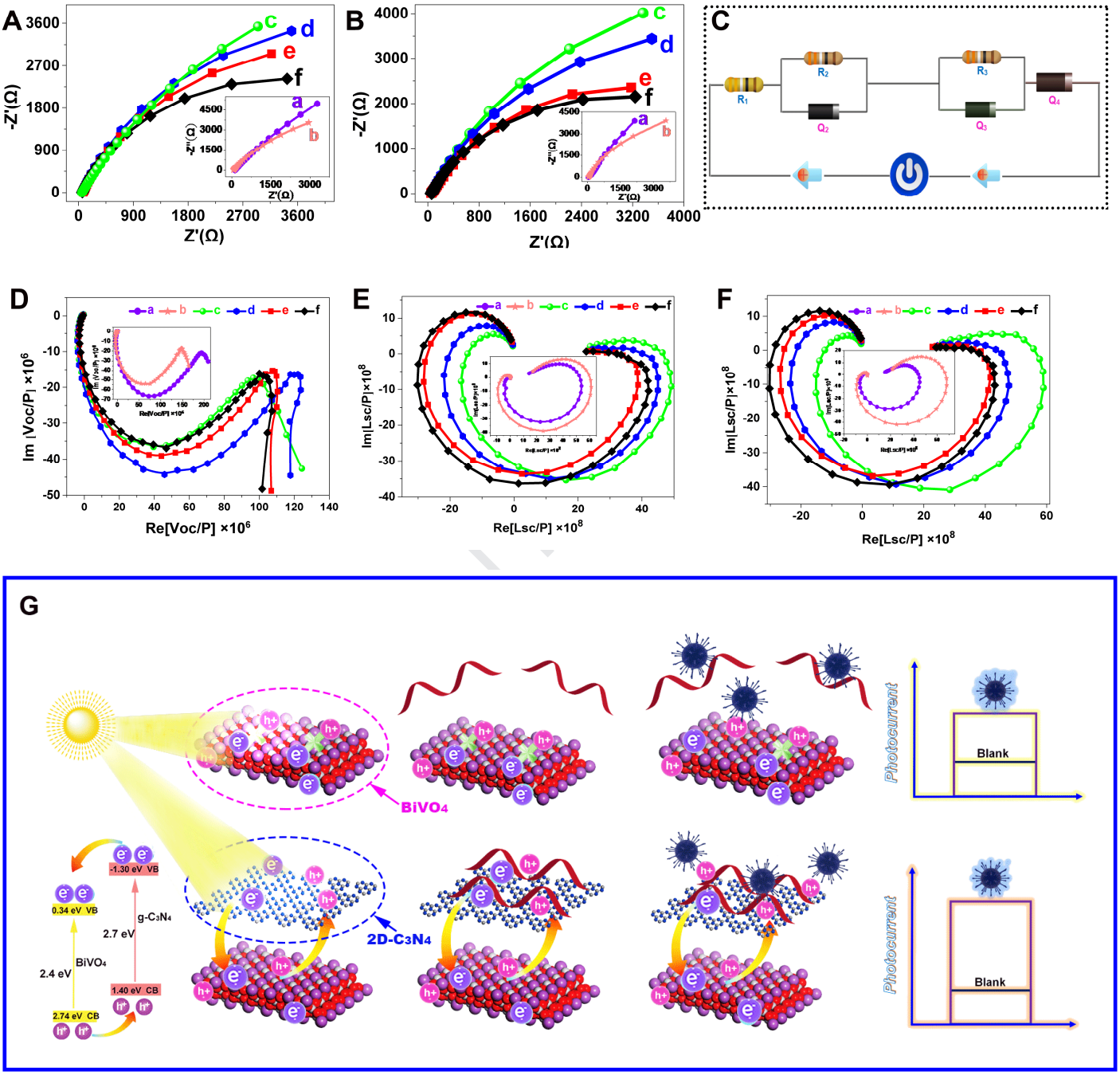

Fig. 4. (A) EIS results of (a) $BiVO_4$, (b) $BiVO_4$/2D-C_3N_4, (c) $BiVO_4$/2D-C_3N_4/DNA aptamer, (d) $BiVO_4$/2D-C_3N_4/DNA aptamer incubated with 5×10^{-7} μg/L MC-LR, (e) with 0.0025 μg/L MC-LR, (f) with 10 μg/L MC-LR at bias potential of 0.05 V under illumination. (B) EIS results of (a) $BiVO_4$, (b) $BiVO_4$/2D-C_3N_4, (c) $BiVO_4$/2D-C_3N_4/DNA aptamer, (d) $BiVO_4$/2D-C_3N_4/DNA aptamer incubated with 5×10^{-7} μg/L MC-LR, (e) with 0.0025 μg/L MC-LR, (f) with 10 μg/L MC-LR at bias potential of 0.1 V under illumination. (C)

Equivalent circuit for EIS results fitting. (D) CIMVS (testing at open circuit potential) of (a) $BiVO_4$, (b) $BiVO_4$/2D-C_3N_4, (c) $BiVO_4$/2D-C_3N_4/DNA aptamer, (d) $BiVO_4$/2D-C_3N_4/DNA aptamer incubated with 5×10^{-7} μg/L MC-LR, (e) with 0.0025 μg/L MC-LR, (f) with 10 μg/L. (E) CIMPS (bias potential 0.05 V) of (a) $BiVO_4$, (b) $BiVO_4$/2D-C_3N_4, (c) $BiVO_4$/2D-C_3N_4/DNA aptamer, (d) $BiVO_4$/2D-C_3N_4/DNA aptamer incubated with 5×10^{-7} μg/L MC-LR, (e) with 0.0025 μg/L MC-LR, (f) with 10 μg/L. (F) CIMPS (bias potential 0.1 V) of (a) $BiVO_4$, (b) $BiVO_4$/2D-C_3N_4, (c) $BiVO_4$/2D-C_3N_4/DNA aptamer, (d) $BiVO_4$/2D-C_3N_4/DNA aptamer incubated with 5×10^{-7} μg/L MC-LR, (e) with 0.0025 μg/L MC-LR, (f) with 10 μg/L. (G) Schematic of photogenerated charge transport process.

3.5 Analysis of real water sample PEC/DNA aptamer sensor for MC-LR and the detection of other biological substances

To verify the practicability and the accuracy of the PEC $BiVO_4$/2D-C_3N_4/DNA aptamer sensor designed in this work, the detective samples were collected from the major freshwater lakes in China (Qinghai Lake, Chao Lake, Dian Lake, Tai Lake) in July 2019. **Fig. S6A** shows the geographic position distribution of the four major lakes; **Fig. S6B** presents the collected water samples and the collection times; **Fig. S6C** shows the photocurrent variation curves of various samples detected by the PEC $BiVO_4$/2D-C_3N_4/DNA aptamer sensor. It can be obtained the information that the MC-LR concentration in Qinghai Lake, Chaohu Lake, Dianchi Lake, and Taihu Lake are 4.78×10^{-6} μg/L, 0.04 μg/L, 1.26 μg/L, and 97.42 μg/L, respectively. These detection results are basically consistent with the ELISA results obtained from a third-party detection institution (Shanghai Jining Shiye, China, Shanghai) (**Table S3**). Because of the LOD (0.017 μg/L) of the ELISA for MC-LR detection, for the water sample from Qinghai Lake, the MC-LR couldn't be detected by the third-party detection institution, however, it was achieved by PEC $BiVO_4$/2D-C_3N_4/DNA aptamer sensor, and the value was 4.78×10^{-6} μg/L. The above results suggested that the high sensitivity detection results tested by the PEC $BiVO_4$/2D-C_3N_4/DNA aptamer sensor are accurate, and it can work accurately in the real natural water environment also.

Lastly, the general applicability of the PEC $BiVO_4$/2D-C_3N_4/DNA aptamer sensor designed in this work was evaluated. Our results suggested that the sensor could be applied in detecting the heavy metal ion, antibiotic and tumor marker, after changing the corresponding DNA aptamer. **Fig. 5A ~ 5C** show the linear detection

lines of Hg^{2+}, tetracycline and dopamine, respectively. Upon calculation, the Hg^{2+} linear detection area is 0.05 fM ~1 μM, and the LOD is 1.43×10^{-17} M . The tetracycline linear detection area is 0.01 pM~1 μM, and the LOD is 2.70 $\times10^{-15}$ M. The dopamine linear detection area is 0.1 pM~0.1 mM, and the LOD is 0.468 $\times10^{-13}$ M. Compared with the similar sensors have been reported to detect the above three substances, the PEC $BiVO_4$/2D-C_3N_4/DNA aptamer sensor designed in this paper shows significant advantage on the sensitivities (Zhao et al., 2015; Chen et al., 2019; H. Li et al., 2017; Zhang et al., 2019; Sultana et al., 2019).

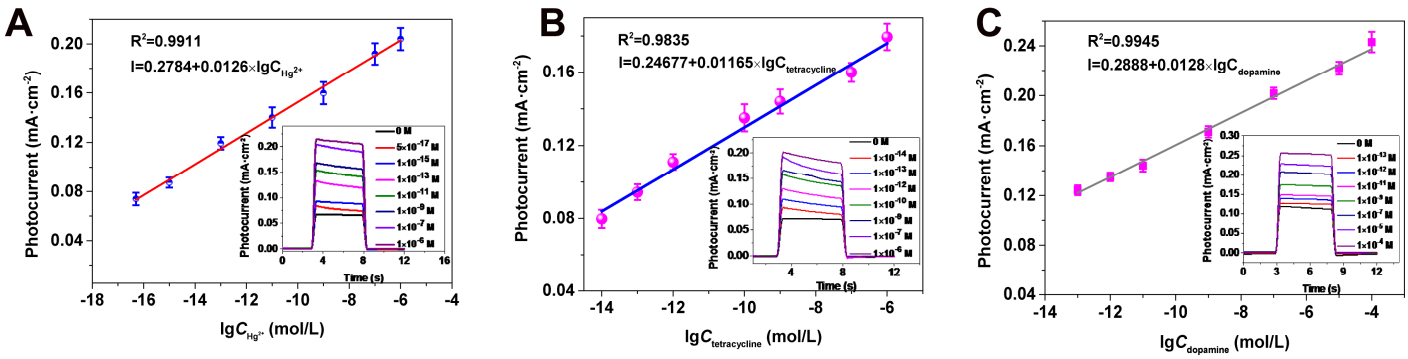

Fig. 5. (A) The corresponding liner calibration cure for different concentrations of Hg^{2+} (5×10^{-17} ~1×10^{-6} M). (B) The corresponding liner calibration cure for different concentrations of tetracycline (1×10^{-14} ~ 1×10^{-6} M). (C) The corresponding liner calibration cure for different concentrations of dopamine (1×10^{-13} ~ 1×10^{-4} M).

Conclusion

In this work, we employed 2D-C_3N_4 as an interlayer material for semiconductor/DNA aptamer interface reconciliation. The fabricated $BiVO_4$/2D-C_3N_4 DNA aptamer sensor achieved a record detective sensitivity for MC-LR (detection interval:5×10^{-7} μg/L ~ 10 μg/L, LOD: 4.191×10^{-8} μg/L). This research provides a new strategy for the multifunctional interface reconcile and some theoretical foundations for highly sensitive PEC semiconductor/DNA aptamer sensors design. In addition, this study provides a new sensitivity level of the semiconductor PEC/DNA aptamer sensor, inducing more possibilities with higher level for the trace substances detection in the fields of environmental monitoring, pathology medicine and non-invasive detection. Up to new, there are some challenges to limit the application of this $BiVO_4$/2D-C_3N_4 DNA aptamer sensor also, such as

complicated fabrication process, relative-high prices of 2D-C_3N_4 and low re-use capacity of the sensor, so that more research should be carried out in the future to solve these challenges.

AUTHOR INFORMATION

Corresponding Author

*E-mail: yybu@xidian.edu.cn

ORCID

https://orcid.org/0000-0001-5601-2877

Notes

The authors declare no competing financial interest.

ACKNOWLEDGMENT

This work was financially supported by the National Natural Science Foundation of China (Grant Nos. 41506093) and Fundamental Research Funds for the Central University and the Innovation Fund of Xidian University.

References

Chang, M.-J., Cui, W.-N., Liu, J., Wang, K., Chai, X.-J., 2018. J. Mater. Sci. Mater. Electron. 29, 6771–6778.

Chen, J., Gao, P., Wang, H., Han, L., Zhang, Y., Wang, P., Jia, N., 2018. J. Mater. Chem. C 6, 3937–3944.

Chen, K., Liu, M., Zhao, G., Shi, H., Fan, L., Zhao, S., 2012. Environ. Sci. Technol. 46, 11955–11961.

Chen, L., Lin, J., Yi, J., Weng, Q., Zhou, Y., Han, Z., Li, C., Chen, J., Zhang, Q., 2019. Anal. Bioanal. Chem. 411, 5277–5285.

Du, X., Jiang, D., Dai, L., Zhou, L., Hao, N., Qian, J., Qiu, B., Wang, K., 2016. Biosens. Bioelectron. 81, 242–248.

Freeman, R., Girsh, J., Willner, I., 2013. ACS Appl. Mater. Interfaces 5, 2815–2834.

Huisman, J., Codd, G.A., Paerl, H.W., Ibelings, B.W., Verspagen, J.M.H., Visser, P.M., 2018. Nat. Rev. Microbiol. 16, 471–483.

Lee, E.-H., Son, A., 2019. Chem. Eng. J. 359, 1493–1501.

Li, H., Zhu, M., Chen, W., Wang, K., 2017. Microchim. Acta 184, 4827–4833.

Li, P., Wang, F., Wei, S., Li, X., Zhou, Y., 2017. Phys. Chem. Chem. Phys. 19, 4405–4410.

Liu, J., Cao, Z., Lu, Y., 2009. Chem. Rev. 109, 1948–1998.

Liu, Q., Huan, J., Hao, N., Qian, J., Mao, H., Wang, K., 2017. ACS Appl. Mater. Interfaces 9, 18369–18376.

Liu, X., Gao, S., Li, X., Wang, H., Ji, X., Zhang, Z., 2019. Ecotoxicol. Environ. Saf. 176, 20–26.

Melissen, S.T.A.G., Steinmann, S.N., Le Bahers, T., Sautet, P., 2016. J. Phys. Chem. C 120, 24542–24550.

Ng, A., Chinnappan, R., Eissa, S., Liu, H., Tlili, C., Zourob, M., 2012. Environ. Sci. Technol. 46, 10697–10703.

Preece, E.P., Hardy, F.J., Moore, B.C., Bryan, M., 2017. Harmful Algae 61, 31–45.

Song, M., Wu, Y., Wang, X., Liu, M., Su, Y., 2018. J. Colloid Interface Sci. 529, 375–384.

Sultana, A., Sazawa, K., Islam, M.S., Sugawara, K., Kuramitz, H., 2019. Anal. Lett. 52, 1153–1164.

Tan, C., Cao, X., Wu, X.-J., He, Q., Yang, J., Zhang, X., Chen, J., Zhao, W., Han, S., Nam, G.-H., Sindoro, M., Zhang, H., 2017. Chem. Rev. 117, 6225–6331.

Tan, F., Saucedo, N.M., Ramnani, P., Mulchandani, A., 2015. Environ. Sci. Technol. 49, 9256–9263.

Tang, X., Yin, Z., Lei, X., Zeng, Y., Zhang, Z., Lu, Y., Zhou, G., Li, L., Wu, X., 2019. Nanomaterials.

Tian, J., Zhao, H., Quan, X., Zhang, Y., Yu, H., Chen, S., 2014. Sensors Actuators B Chem. 196, 532–538.

Tian, N., Zhang, Y., Li, X., Xiao, K., Du, X., Dong, F., Waterhouse, G.I.N., Zhang, T., Huang, H., 2017. Nano Energy 38, 72–81.

Wang, Y., Sun, J., Li, J., Zhao, X., 2017. Langmuir 33, 4694–4701.

Wei, J., Chang, W., Qileng, A., Liu, W., Zhang, Y., Rong, S., Lei, H., Liu, Y., 2018. Anal. Chem. 90, 9606–9613.

Wu, J., Xianyu, Y., Wang, X., Hu, D., Zhao, Z., Lu, N., Xie, M., Lei, H., Chen, Y., 2018. Anal. Chem. 90, 4725–4732.

Yalavarthi, R., Naldoni, A., Kment, Š., Mascaretti, L., Kmentová, H., Tomanec, O., Schmuki, P., Zbořil, R., 2019. Catalysts 9.

Zervou, S.-K., Christophoridis, C., Kaloudis, T., Triantis, T.M., Hiskia, A., 2017. J. Hazard. Mater. 323, 56–66.

Zhang, J., Ren, F., Deng, M., Wang, Y., 2015. Phys. Chem. Chem. Phys. 17, 10218–10226.

Zhang, X., Yan, T., Wu, T., Feng, Y., Sun, M., Yan, L., Du, B., Wei, Q., 2019. Biosens. Bioelectron. 135, 88–94.

Zhang, X., Zhao, Y., Li, S., Zhang, S., 2010. Chem. Commun. 46, 9173–9175.

Zhao, M., Fan, G.-C., Chen, J.-J., Shi, J.-J., Zhu, J.-J., 2015. Anal. Chem. 87, 12340–12347.

Zhao, W.-W., Xu, J.-J., Chen, H.-Y., 2014. Chem. Rev. 114, 7421–7441.

Zhou, H., Liu, J., Zhang, S., 2015. TrAC Trends Anal. Chem. 67, 56–73.

HIGHLIGHTS

1. Novel PEC $BiVO_4$/2D-C_3N_4/ DNA aptamer sensor has been fabricated.
2. Record sensitivity for Microcystin-LR detection.
3. 2D-C_3N_4 provides a multifunctional reconciliation of the $BiVO_4$/DNA interface.
4. The sensor shows large application width for trace substances detection.

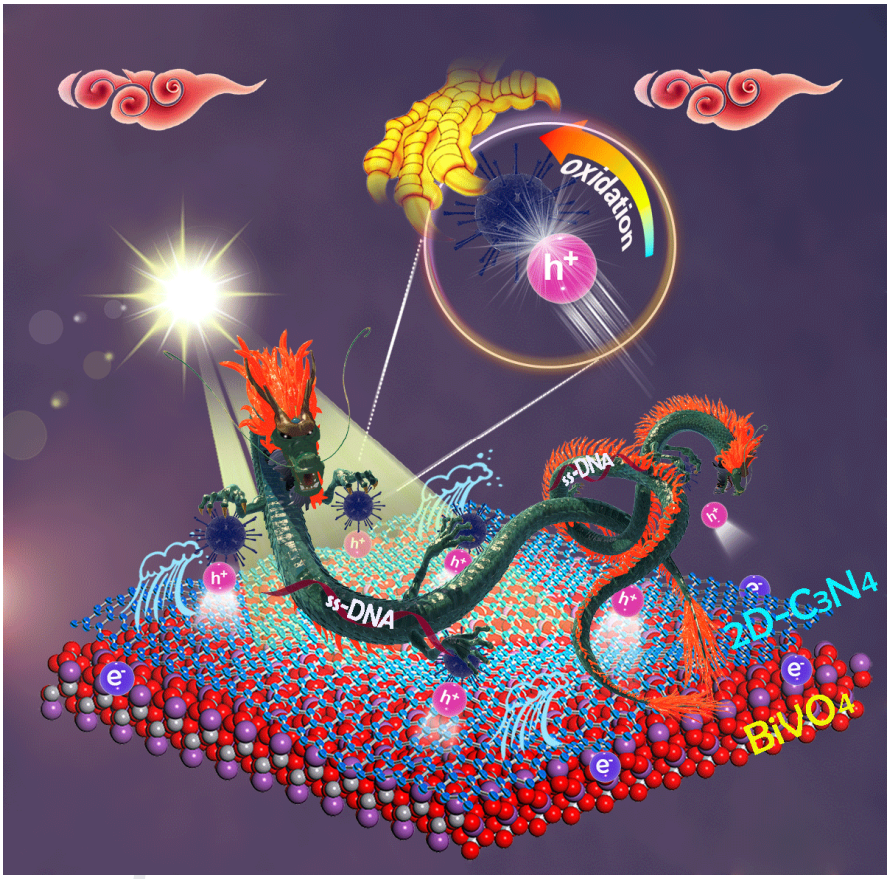

The article is original and has been written by all the stated authors who are all-aware of its content and approve its submission. It has not been published previously and it is not under consideration for publication elsewhere. No conflict of interest exists for all authors and if accepted, the article will not be published elsewhere in the same form.